

**In-situ study of rules of nanostructure evolution, severe plastic deformations, and friction under high pressure**

*Feng Lin\*, Valery I. Levitas\*, Krishan K. Pandey, Sorb Yesudhas, and Changyong Park*

F. Lin

Department of Aerospace Engineering, Iowa State University, Ames, Iowa 50011,  
USA

E-mail: [flin1@iastate.edu](mailto:flin1@iastate.edu)

V. I. Levitas

Department of Aerospace Engineering, Iowa State University, Ames, Iowa 50011,  
USA

Department of Mechanical Engineering, Iowa State University, Ames, Iowa 50011,  
USA

Ames Laboratory, U.S. Department of Energy, Iowa State University, Ames, Iowa  
50011, USA

E-mail: [vlevitas@iastate.edu](mailto:vlevitas@iastate.edu)

K. K. Pandey

High Pressure & Synchrotron Radiation Physics Division, Bhabha Atomic Research  
Centre, Mumbai 400085, India

Email: [kkpandey@barc.gov.in](mailto:kkpandey@barc.gov.in)

S. Yesudhas

Department of Aerospace Engineering, Iowa State University, Ames, Iowa 50011,  
USA

Email: [sorbya@iastate.edu](mailto:sorbya@iastate.edu)

C. Park

HPCAT, X-ray Science Division, Argonne National Laboratory, Argonne, Illinois  
60439, USA

Email: [cypark@anl.gov](mailto:cypark@anl.gov)

Keywords: high pressures, severe plastic deformations, in-situ synchrotron  
diffraction, yield strength, nanostructure evolution

## **Abstract**

Severe plastic deformations under high pressure are used to produce nanostructured materials but were studied ex-situ. We introduce rough diamond anvils to reach maximum friction equal to yield strength in shear and perform the first in-situ study of the evolution of the pressure-dependent yield strength and nanostructural parameters for severely pre-deformed Zr.  $\omega$ -Zr behaves like perfectly plastic, isotropic, and strain-path-independent. This is related to reaching steady values of the crystallite size and dislocation density, which are pressure-, strain- and strain-path-independent. However, steady states for  $\alpha$ -Zr obtained with smooth and rough anvils are different, which causes major challenge in plasticity theory.

## **Impact statement**

In-situ study of severe plastic deformation of  $\omega$ -Zr with rough diamond anvils revealed that pressure-dependent yield strength, crystallite size, and dislocation density are getting steady and plastic strain- and strain-path-independent.

## **1. Introduction**

Processes involving severe plastic deformations under high pressure are common in producing nanostructured materials [1-8], in functional materials experiencing extreme stresses under contact friction, collision, and penetration, as well as in geophysical processes [9,10]. The effects of severe plastic deformations under high

pressure on microstructure evolution are mostly studied with high-pressure torsion (HPT) with metallic or ceramic anvils [1-4]. Stationary states after severe plastic straining in terms of torque, hardness, grain size, and dislocation density are well-known in literature, particularly after HPT, along with many cases where they were not observed [1-8]. However, all these results *were not observed in-situ but obtained postmortem* after pressure release and further treatment during sample preparation for mechanical and structural studies. The only paper [11] studies the dislocation density and crystallite size in Ni during HPT in a single peripheral region in situ, while pressure was still determined as force divided by area, which may strongly deviate from the local pressure in the studied region. Also, the beam passes through a significant protrusion part of a sample, which underwent relatively small plastic strain under compression and had lower and very heterogeneous stresses, bringing essential inaccuracy. The direct effect of pressure and the combined effect of pressure and plastic straining on the yield strength, crystallite size, and dislocation density were not determined in the literature. This is very important because, as we will see, the yield strength of the  $\omega$ -Zr doubles at  $\sim 13$  GPa. It is shown in [11] that during pressure release after HPT of Ni, crystallite size increases, and dislocation density decreases by a factor of 2. Similar results were obtained for Zr under hydrostatic loading [12]. Note that importance of in-situ molecular dynamics analysis versus ex-situ experiments was stressed in [13].

Generally, a robust method for measurement of the yield strength in compression  $\sigma_y(p)$  under high pressure  $p$  is lacking. The main difficulty in studying plasticity, structural changes, and contact friction is that they depend on five components of the plastic strain tensor  $\boldsymbol{\varepsilon}_p$  and its entire path  $\boldsymbol{\varepsilon}_p^{path}$ , making an unspecifiable number of combinations of independent parameters. For example, compression then shear or shear then compression to the same  $\boldsymbol{\varepsilon}_p$  lead to different stresses. In particular, the yield surface in the 5D deviatoric stress  $\boldsymbol{s}$  space  $f(\boldsymbol{s}, \boldsymbol{\varepsilon}_p, \boldsymbol{\varepsilon}_p^{path}) = \sigma_y(p)$  depends on  $p$ ,  $\boldsymbol{\varepsilon}_p$ , and  $\boldsymbol{\varepsilon}_p^{path}$ , demonstrating strain hardening/softening and strain-induced anisotropy. This complexity makes it

practically impossible to determine the complete evolution of the yield surface, even at small strains at ambient condition. For measurement of yield strength at high pressure, all methods [14-16] treat the yield surface as  $f(\mathbf{s}) = \sigma_y(p)$ , i.e., like for perfectly plastic material (for which the yield surface is independent of  $\boldsymbol{\varepsilon}_p$  and  $\boldsymbol{\varepsilon}_p^{path}$ , i.e., is fixed in the 5D stress space), and dependence on  $\boldsymbol{\varepsilon}_p$  and  $\boldsymbol{\varepsilon}_p^{path}$  is neglected and merged in pressure, which causes large error in the determination of the yield strength under high pressure. One of the methods to determine the yield strength in shear  $\tau_y = \sigma_y/\sqrt{3}$  in diamond anvil cell (DAC) is based on the application of the simplified equilibrium equation  $\frac{d\bar{P}}{dr} = -\frac{2\tau_f}{h}$ , assuming the contact friction stress  $\tau_f$  between anvil and sample reaches its maximum value  $\tau_y$  [15-17] (see supplementary material for detail). Here,  $\bar{P}$  is the pressure averaged over the sample thickness  $h$ . However, the results are systematically lower than other methods at ambient and high pressure [14, 18] due to the low friction coefficient of the diamond leading to  $\tau_f < \tau_y$ . Coupled simulations and experiments show that  $\tau_f = \tau_y$  only in a small region, even above 100 GPa [19]. We introduce *rough diamond anvil (rough-DA)*, whose culet is roughly polished to increase friction (Figure 1). We demonstrated that maximum friction  $\tau_f = \tau_y$  is reached for rough-DA, which allowed us to robustly determine  $\sigma_y(p)$  and plastic friction.

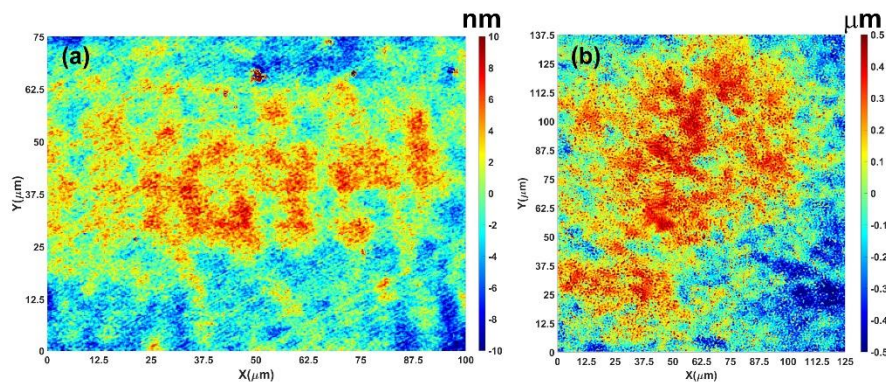


**Figure 1. Surface asperity profile of a smooth anvil and a rough-DA.** (a) Traditional smooth diamond anvil with an asperity profile range [-10 nm; 10 nm] and (b) rough-polished diamond anvil (rough-DA) with a range [-500 nm; 500 nm].

It was hypothesized in [17] that, above some level of accumulated plastic strain  $q$  in monotonous straining (straining path without sharp changes in directions), the initially isotropic polycrystalline materials deform as perfectly plastic and isotropic with a strain path-independent surface of the perfect plasticity  $\varphi(\mathbf{s}) = \sigma_y(p)$  (Figure 2). This statement means that the effect of  $\boldsymbol{\varepsilon}_p$  and  $\boldsymbol{\varepsilon}_p^{path}$  is excluded under the above conditions, and reasons for strain-induced anisotropy disappear. Some qualitative supportive arguments for the perfect plastic behavior are presented in [17], but the quantitative experimental proof is lacking for any material. Here, we severely pre-deformed commercial Zr by multiple rolling until saturation of its hardness. We show that after the  $\alpha$ - $\omega$  phase transformation, for four different compression stages (i.e., for very different  $\boldsymbol{\varepsilon}_p$  and  $\boldsymbol{\varepsilon}_p^{path}$ ), all pressure distributions of  $\omega$ -Zr in the studied range from 2 to 11 GPa are described by single function  $\sigma_y = 1.24 + 0.0965(16)p$  (GPa). This is possible only if the *material behaves like perfectly plastic, isotropic, and independent of  $\boldsymbol{\varepsilon}_p$  and  $\boldsymbol{\varepsilon}_p^{path}$* . Similarly, friction stress  $\tau_f = \tau_y = 0.72 + 0.0557(9)p$  (GPa) is also *independent of  $\boldsymbol{\varepsilon}_p$  and  $\boldsymbol{\varepsilon}_p^{path}$* . The perfectly plastic state is related to reaching a steady nanostructure, determined here by in situ synchrotron X-ray diffraction in terms of crystallite (grain) size  $d$  and dislocation density  $\rho$ , which do not change under successive plastic straining. For rough-DA in  $\alpha$ -Zr at the beginning of  $\alpha$ - $\omega$  transformation,  $d_\alpha$  is smaller, and  $\rho_\alpha$  is larger than those from smooth anvils, i.e., *rough-DA produces a different, more refined steady nanostructure*. At the same time, the steady nanostructure for  $\omega$ -Zr after transformation is the same for smooth and rough-DAs.

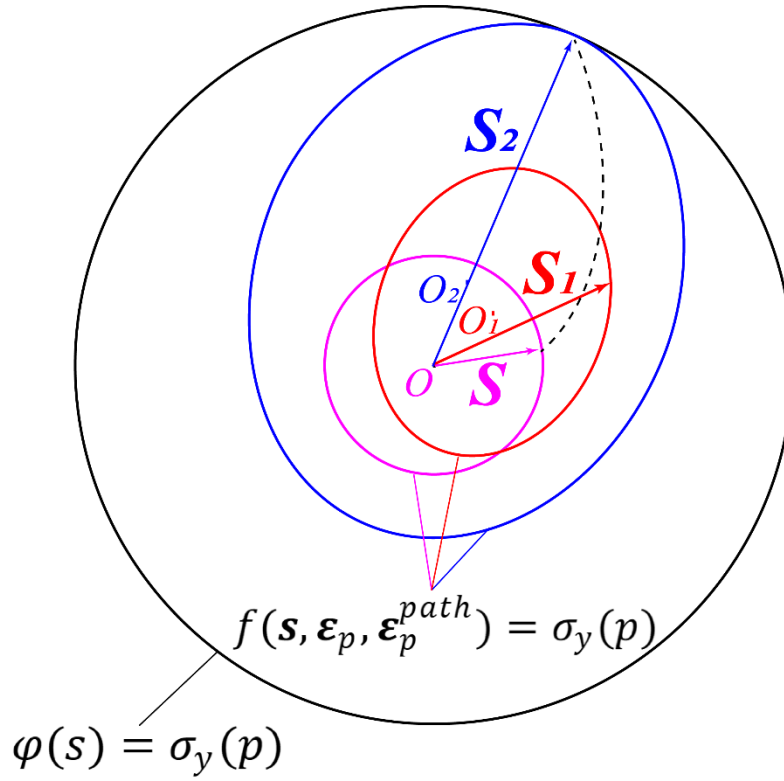


**Figure 2. Evolving yield surface and fixed surface of perfect plasticity.** Schematic of the evolution of the yield surface  $f(\mathbf{s}, \boldsymbol{\varepsilon}_p, \boldsymbol{\varepsilon}_p^{path}) = \sigma_y(p)$  until it reaches the fixed surface of perfect plasticity  $\varphi(\mathbf{s}) = \sigma_y(p)$  in “5D” space of deviatoric stresses  $\mathbf{s}$  at fixed  $p$ . The initial yield surface and  $\varphi(\mathbf{s}) = \sigma_y(p)$  are isotropic (circles). Two other yield surfaces depend on  $\boldsymbol{\varepsilon}_p$  and  $\boldsymbol{\varepsilon}_p^{path}$ , and acquire strain-induced anisotropy, namely shifted centers  $O_1$  and  $O_2$  (back stress) and ellipsoidal shape due to texture. When the yield surface reaches  $\varphi(\mathbf{s}) = \sigma_y(p)$ , the material deforms like perfectly plastic, isotropic with the fixed surface of perfect plasticity.

## 2. Materials and methods

Rough-DAs were introduced and utilized to increase contact friction with a sample. Due to the large asperities of the rough-DA (Figure 1), when they penetrate Zr surface, contact sliding occurs in a thin layer of Zr, leading to  $\tau_f = \tau_y$ . The material in this study is commercially pure (99.8%)  $\alpha$ -Zr (Fe: 330 ppm; Mn: 27 ppm; Hf: 452 ppm; S: <550 ppm; Nd: <500 ppm). We chose Zr as our first test material since Zr and its alloy are widely used in the aerospace, military, medical, and nuclear industries experiencing potential high-pressure environments. We heavily pre-deformed the Zr

slab with an initial thickness of 5.25 mm by multiple rolling down to 163-165  $\mu\text{m}$  until saturation of its hardness. 3 mm diameter disks were punched out from thin foil for unconstrained non-hydrostatic compression in DAC with rough-DAs, and traditional smooth anvils for comparison. The pressure distribution is determined using measured lattice parameters through the 3<sup>rd</sup> order Birch-Murnaghan equation of state of Zr from [18]. The Zr samples were compressed gradually up to  $\sim$ 14-15 GPa at the culet center. In-situ synchrotron XRD experiments in axial diffraction geometry were performed at 16-BM-D beamline at HPCAT (Sector 16) at Advanced Photon Source employing focused monochromatic x-rays of wavelength 0.3100 Å and size of  $6\mu\text{m} \times 5\mu\text{m}$  (full width at half maximum (FWHM)) and recorded with Perkin Elmer detector. The sample disk compressed with rough-DAs was scrutinized along two perpendicular culet diameters (230  $\mu\text{m}$ ) in 10  $\mu\text{m}$  step size. The sample thickness during compression (see Table 1) was measured through x-ray intensity absorption using the linear attenuation equation with density corrected to the corresponding pressure, similar to [18]. The diffraction images were first converted to unrolled patterns using FIT2D software [20] and then analyzed through Rietveld refinement using MAUD software [21] to obtain the lattice parameters, volume fractions of  $\omega$ -Zr, microstrains, and crystallite sizes. Crystallite size and microstrain are used to estimate dislocation density using Williamson-Smallman method [22] (See supplementary material for detail).

**Table 1.** The thickness of Zr sample compressed with rough-DAs at corresponding compression steps marked by the peak pressure at the culet center.

<b>Compression step</b>	initial	3 GPa	6 GPa	10 GPa	14 GPa
<b>Thickness (<math>\mu\text{m}</math>)</b>	163	48	40	32	26

### 3. Results and Discussion

#### 3.1. Perfectly plastic, isotropic, and strain-path-independent behavior of $\omega$ -Zr

We first assume and then will prove that after severe plastic deformation and phase transformation, the initially isotropic polycrystalline Zr deforms as perfectly plastic and isotropic with a strain path-independent surface of the perfect plasticity  $\varphi(\mathbf{s}) = \sigma_y(p)$  (Figure 2). To determine the pressure dependence of the yield strength of  $\omega$ -Zr, the pressure distribution of fully transformed region can be used only, i.e., region around culet center of 3 GPa step and the whole diameters after 3 GPa step. Assuming von Mises yield condition with  $\sigma_y = \sigma_y^0 + bp$ , and taking non-hydrostatic stress and heterogeneity along thickness into consideration, the equilibrium equation averaged over thickness is advanced to (see supplementary material):

$$\frac{d\bar{P}}{dr} = -A \frac{\sigma_y^0 + b\bar{P}}{h} \rightarrow \bar{P} = (P_0 + \frac{\sigma_y^0}{b}) \exp\left(-A b \frac{r-r_0}{h}\right) - \frac{\sigma_y^0}{b}; A = \frac{2(1+0.524b)}{\sqrt{3}(1-0.262b)}, \quad (1)$$

where  $\bar{P}$  and  $P_0$  are the pressure averaged over the sample thickness and at the point  $r_0$ , respectively. From equation (1),

$$\sigma_y(\bar{P}) = -Ah \frac{d\bar{P}}{dr} = -A \frac{d\bar{P}}{d(\frac{r}{h})}. \quad (2)$$

The pressure distributions are plotted as a function of dimensionless normalized radial position  $r/h$  in Figure 3. To extract the yield strength utilizing data at all compression steps and positions, pressure distributions from different compression stages are shifted horizontally to the same position. Figure 3 shows that for four different compression stages all pressure distributions overlap with each other and are described by Equation (1) with single pressure dependence  $\sigma_y = 1.24 + 0.0965(16)p$  (GPa). Note that  $\sigma_y^0 = 1.24$  GPa is converted from the hardness of  $\omega$ -Zr from [23],  $H=3.72$  GPa, based on the known relationship  $\sigma_y^0 = H/3$ , proving that  $\tau_y$  is reached with rough-DA. Finite element simulations of the processes in DAC [19, 24, 25] (and Figure S1) demonstrate that for different material positions and compression stages,  $\boldsymbol{\varepsilon}_p$ ,  $\boldsymbol{\varepsilon}_p^{path}$ , and material rotations vary substantially.

Consequently, the ability to describe all four curves with single function  $\sigma_y(p)$  demonstrates strict proof, for the first time, that for the monotonous loading with rough-DAs,  $\omega$ -Zr deforms as perfectly plastic and isotropic material with  $\boldsymbol{\varepsilon}_p$  and



$\epsilon_p^{path}$  independent surface of perfect plasticity. Similar, friction stress  $\tau_f = \tau_y = \frac{\sigma_y}{\sqrt{3}} = 0.72 + 0.0557(9)p$  (GPa) is also independent of  $\epsilon_p$  and  $\epsilon_p^{path}$ . We also found that for smooth anvils up to 15 GPa, the ratio  $\tau_f/\tau_y = 0.39-0.46$  away from the center characterizes underestimate in the  $\sigma_y(p)$  in previous works [15-17]. Note that the steady state in the yield strength does not correspond to the steady state in torque in high-pressure torsion [26], mostly due to the complexity of the friction condition.

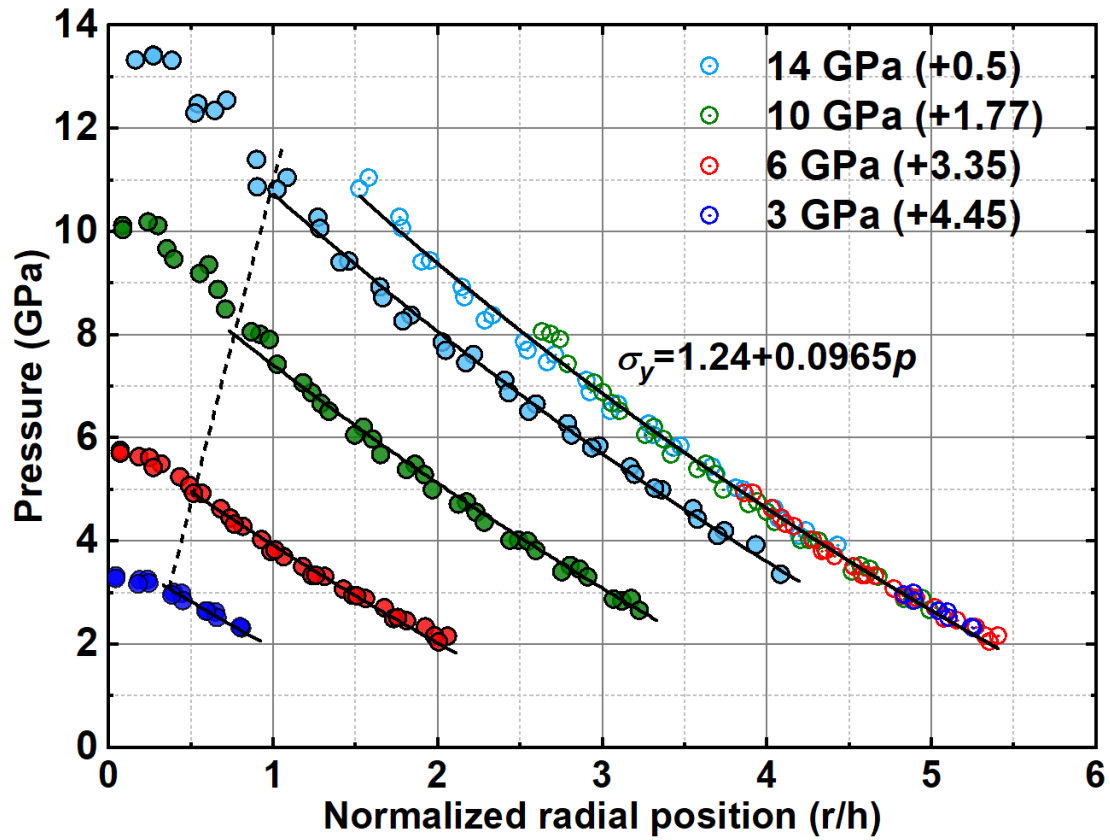


**Figure 3. Pressure in single-phase  $\omega$ -Zr vs.  $r/h$ .** Solid lines correspond to Equation (1) for  $\sigma_y^0 = 1.24$  GPa and  $b=0.0965$ . Equation (1) is not valid around the culet center due to reduction in friction stress to zero at the symmetry axis. Dash line shows the position where data is truncated. The unified curve for all loadings (necessary for using data from all four compression stages as a single data set) is obtained by shifting each curve (which is allowed by differential Equation (1), see supplementary material) along the horizontal axis by an appropriate distance. Shifts are shown in parentheses. Since for different points from different curves  $\epsilon_p$ ,  $\epsilon_p^{path}$ , and material rotations vary substantially, the

obtained results prove the existence of perfectly plastic and isotropic material response with  $\epsilon_p$  and  $\epsilon_p^{path}$  independent surface  $\varphi(\mathbf{s}) = \sigma_y(p)$ . Note that uncertainty of pressure as well as crystallite size and dislocation density in the following are smaller than the symbols.

### 3.2. Steady plastic strain, strain path, and pressure independent nanostructure in $\omega$ -Zr

We connect perfectly plastic behavior with reaching steady nanostructure. After completing phase transformation in the whole sample, crystallite size  $d_\omega$  for 6, 10, and 14 GPa steps scatters between 40 and 60 nm, being practically independent of radius (Figure 4(a)). Dislocation density  $\rho_\omega = 1.04(19) \times 10^{15} \text{m}^{-2}$  is also being practically independent of radius (Figure 4(b)). Since  $\epsilon_p$ ,  $\epsilon_p^{path}$ , and  $p$  strongly vary with radius and increasing load, this indicates that steady nanostructure, which is independent of pressure,  $\epsilon_p$ , and  $\epsilon_p^{path}$ , is reached. Note that in [13], steady yield strength and dislocation density independent of the changes in strain rate path were obtained in molecular dynamics simulations for a single crystal Ta. These results were called “a tantalizing general hypothesis that merits further scrutiny.”

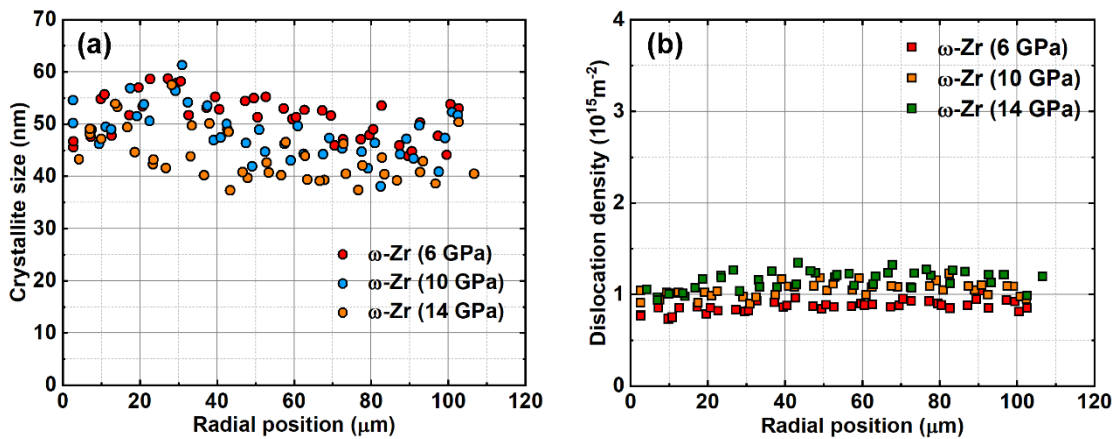


**Figure 4. Radial distribution of the crystallite size (a) and dislocation density (b) in  $\omega$ -Zr for three loading steps after full transformation.** Since  $\epsilon_p$ ,  $\epsilon_p^{path}$ , and  $p$  strongly vary with radius and increasing load, approximate independence of  $d_\omega$  and  $\rho_\omega$  of radius and load indicates that steady

nanostructure in terms of crystallite size and dislocation density, which is independent of pressure,  $\epsilon_p$ , and  $\epsilon_p^{path}$ , is reached.

### 3.3. Multiple steady states for $\alpha$ -Zr

For  $\omega$ -Zr, with smooth and rough-DA, the steady dislocation densities,  $0.95(5)\times 10^{15}\text{m}^{-2}$  and  $1.04(19)\times 10^{15}\text{m}^{-2}$ , respectively, are practically the same; the crystallite sizes, 49(1) nm and 47(6) nm, respectively, are the same as well. This is because plastic strain during reaching 15 GPa with smooth anvils is large enough. A completely different situation is with  $\alpha$ -Zr, which has three steady states:

1. After multiple rolling at ambient pressure, with  $\rho_\alpha = 1.00(2)\times 10^{15}\text{m}^{-2}$  and  $d_\alpha \approx 75(1)$  nm;
2. After deformation with smooth anvils, just before initiation of the  $\alpha$ - $\omega$  phase transformation at 1.36 GPa, with  $\rho_\alpha = 1.26(7)\times 10^{15}\text{m}^{-2}$  and  $d_\alpha \approx 65(1)$  nm;
3. After deformation with rough-DA, just before initiation of the  $\alpha$ - $\omega$  transformation at 0.67 GPa, with  $\rho_\alpha = 1.84(3)\times 10^{15}\text{m}^{-2}$  and  $d_\alpha \approx 48(2)$  nm.

The reason for different steady states cannot be related to the different pressures only. Indeed, with increasing pressure, the crystallite size decreases, and dislocation density increases [11, 12], while here, results with smooth and rough-DA have the opposite trend. Our results about the existence of multiple steady states are consistent with known results that different ways to produce severe plastic deformation (e.g., HPT, equal channel extrusion, ball milling, etc.) lead to different steady grain sizes [1-3]. However, different steady dislocation density and crystallite size mean different yield strengths  $\sigma_y^i(p)$  (which we could not determine robustly due to the small number of experimental points for single-phase  $\alpha$ -Zr) and surfaces of perfect plasticity  $\varphi^i(s) = \sigma_y^i(p)$  (Figure 5). Each of these states was obtained at quite different plastic strain and strain paths, so each of them supposed to be independent of  $\epsilon_p$  and  $\epsilon_p^{path}$ . But if this is true, how can steady  $\rho$ ,  $d$ , and  $\sigma_y^i(p)$  be different, and which of these steady

values should be used in plasticity theory, particularly for the surfaces of perfect plasticity? Thus, the existence of multiple steady states leads to the formulation of a new major challenge in the plasticity and microstructure evolution theories. Thus, the key problem is: for which classes of  $\epsilon_p$  and  $\epsilon_p^{path}$  and may be pressure path, material behaves along each of the surfaces  $\varphi^i(s) = \sigma_y^i(p)$  with corresponding steady dislocation density and crystallite sizes, and for which loading classes the material behavior jumps from one surface to another with different steady dislocation density and crystallite sizes? When this problem is resolved, one will be able to also explain why different severe plastic deformation technologies, like HPT, equal channel extrusion, ball milling, etc., lead to different steady grain sizes and dislocation densities [1-3], and how to design the loading paths to reduce the grain size and increase dislocation density and strength?

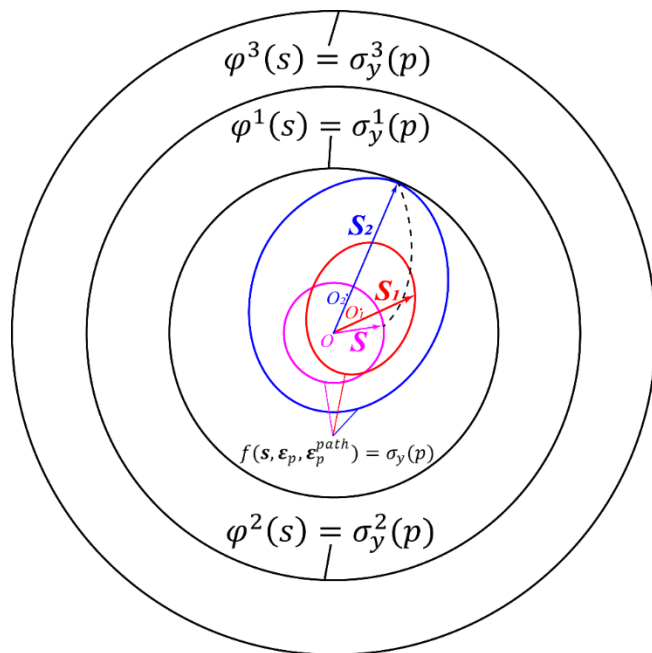


**Figure 5. Evolving yield surface and several fixed surfaces of perfect plasticity.** Part of the schematic with the internal fixed surface of perfect plasticity  $\varphi^1(s) = \sigma_y^1(p)$  in "5D" space of deviatoric stresses  $\mathbf{s}$  at fixed  $p$  coincides with that in Figure 2. The difference is in the presence of several other fixed surfaces of perfect plasticity  $\varphi^i(s) = \sigma_y^i(p)$  with larger yield strength  $\sigma_y^i(p)$ . This

raises the key problem: for which classes of  $\epsilon_p$  and  $\epsilon_p^{path}$ , and may be pressure path, material behaves along each of the surfaces of perfect plasticity  $\phi^i(s) = \sigma_y^i(p)$ , and for which loading classes the material behavior jumps from one surface to another with different steady dislocation density and crystallite sizes?

#### 4. Concluding remarks

In this paper, the *first in-situ* study of the rules of dislocation density, crystallite size, yield surface, and contact friction under high pressure and severe plastic deformation is presented. Very simple rules were found that after some critical plastic strain,  $\omega$ -Zr behaves like perfectly plastic and isotropic, with fixed plastic strain and the strain-path-independent surface of the perfect plasticity  $\phi(s) = \sigma_y(p)$ . The perfectly plastic behavior is connected to another rule: crystallite size and dislocation density of  $\alpha$  and  $\omega$ -Zr are getting  $p$ ,  $\epsilon_p$  and  $\epsilon_p^{path}$ -independent and reach steady values.

To provide a robust method to determine  $\sigma_y(p)$  and plastic friction stress for  $\omega$ -Zr, we introduce *rough-DA* with increased height of asperities. We demonstrated that maximum friction  $\tau_f = \tau_y$  is reached for rough-DAs. We also advanced the simplified equilibrium equation by including the variation of stresses along the thickness and utilized data after reaching perfectly plastic strain only, thus avoiding mixing of the effect of  $\epsilon_p$  and  $\epsilon_p^{path}$  and pressure. That is why the found relationship,  $\sigma_y = 1.24 + 0.0965(16)p$  (GPa), is much more precise than could be obtained with previous methods. In particular, for smooth anvils up to 15 GPa, the ratio  $\tau_f/\tau_y = 0.39-0.46$  characterizes an underestimate in the  $\sigma_y(p)$  in previous works [15-17]. Reaching  $\tau_f = \tau_y$  immediately implies that the plastic friction  $\tau_f = \tau_y = 0.72 + 0.0557(9)p$  (GPa) is also *independent of  $\epsilon_p$  and  $\epsilon_p^{path}$* .

While steady nanostructure for  $\omega$ -Zr is the same for smooth and rough-DAs, for  $\alpha$ -Zr rough-DAs produce smaller crystallite size  $d_\alpha$  and larger dislocation density  $\rho_\alpha$  than those with smooth anvils, i.e., *rough-DAs produce different, more refined*

*steady nanostructure*. After multiple rolling, one more steady nanostructure with larger  $d_\alpha$  and smaller  $\rho_\alpha$  also appears different. Since each of them along with different corresponding yield strengths are independent of  $\epsilon_p$  and  $\epsilon_p^{path}$ , the new key problem in plasticity theory is formulated: for which classes of  $\epsilon_p$ ,  $\epsilon_p^{path}$ , and may be pressure path material behaves along each of the surfaces  $\varphi^i(s) = \sigma_y^i(p)$  and for which loading classes the material behavior jumps from one surface to another? Solution to this problem will allow one to explain why different severe plastic deformation technologies lead to different steady grain sizes and dislocation densities and how to design the loading paths to reduce the grain size and increase dislocation density and strength. Similar studies can be repeated for any other material system.

Obtained results suggest a potentially more economical way to produce the desired steady nanostructure with rough-DAs. Thus, instead of severe plastic straining at high pressure, e.g., by HPT, one can reach one of the steady nanostructures by severe straining at normal pressure (e.g., by rolling or equal channel extrusion) and then reach steady nanostructure with smaller grain size at relatively small plastic strain and low pressure by compression without or with HPT. Rough-DAs also reduce the phase transformation pressure, which will be discussed in future work. Also, rough-DAs eliminate the problem of describing contact friction required for modeling deformational processes in DAC [19, 24, 27]. For traditional HPT with ceramic/metallic anvils, friction reaches the maximum possible level due to large asperities. Utilizing rough-DAs in rotational DAC [28-30] will allow in-situ studies of HPT. In addition, to increase the maximum possible pressure in DAC, toroidal grooves are used [31], which increase friction [17]. This can be done with rough-DAs more uniformly throughout the culet and with smaller stress concentrators.

Importantly, our findings are formulated in the language of plasticity theory (plastic strain and strain path tensors, yield surface, etc.) instead of technological language, which allows one to use the obtained knowledge to significantly enrich fundamental plasticity in the formulation and application of plastic models to various processes. Note that the above plethora of results was obtained in a single experiment,

thus transforming the main experimental challenge—strongly heterogeneous fields—into a great opportunity.

### Acknowledgements

The authors thank (a) Drs. Alexander Zhilyaev and María Teresa Pérez-Prado for providing Zr sample; (b) Dr. Reinhard Boehler for preparing the surface of rough-DA; (c) Dr. Ashraf Bastawros and Dr. Bishoy Dawood for the help with asperity measurement. Support from NSF (CMMI-1943710 and DMR-1904830), and Iowa State University (Vance Coffman Faculty Chair Professorship) is greatly appreciated. This work is performed at HPCAT (Sector 16), Advanced Photon Source (APS), Argonne National lab. HPCAT operations are supported by DOE-NNSA's Office of Experimental Science. The Advanced Photon Source is a U.S. Department of Energy (DOE) Office of Science User Facility operated for the DOE Office of Science by Argonne National Laboratory under Contract No. DE-AC02-06CH11357.

### **Conflict of interest**

The authors declare no competing interests.

### **Data availability**

The data that support the findings of this study are available from the corresponding authors upon request.

### **Reference**

1. Edalati K, Bachmaier A, Beloshenko VA, et al. Nanomaterials by severe plastic deformation: review of historical developments and recent advances. *Mater. Res. Lett.* 2022; 10(4):163-256.

2. Edalati K, Horita K. A review on high-pressure torsion (HPT) from 1935 to 1988. *Mater. Sci. Eng., A*. 2016; 652:325-352.
3. Razumov, IK, Yermakov AY, Gornostyrev YN, et al. Nonequilibrium phase transformations in alloys under severe plastic deformation. *Phys.-Usp.* 2020; 63(8):733.
4. Cao Y, Ni S, Liao X, et al. Structural evolutions of metallic materials processed by severe plastic deformation. *Mater. Sci. Eng. R Rep.* 2018; 133:1-59.
5. Valiev RZ, Estrin Y, Horita Z, et al. Producing bulk ultrafine-grained materials by severe plastic deformation. *JOM* 2006; 58:33-39.
6. Ovid'Ko IA, Valiev RZ, Zhu YT. Review on superior strength and enhanced ductility of metallic nanomaterials. *Prog. Mater. Sci.* 2018; 94:462-540.
7. Valiev RZ, Estrin Y, Horita Z, et al. Producing bulk ultrafine-grained materials by severe plastic deformation: ten years later. *JOM* 2016; 68:1216-1226.
8. Zhu YT, Langdon TG. The fundamentals of nanostructured materials processed by severe plastic deformation. *JOM* 2004; 56(10):58-63.
9. Girard J, Amulele G, Farla R, et al. Shear deformation of bridgmanite and magnesiowüstite aggregates at lower mantle conditions. *Science* 2016; 351(6269):144-147.
10. Levitas VI. Resolving puzzles of the phase-transformation-based mechanism of the strong deep-focus earthquake. *Nat. Commun.* 2022; 13(1):6291.
11. Kerber MB, Spieckermann F, Schuster R, et al. In Situ Synchrotron X-Ray Diffraction during High-Pressure Torsion Deformation of Ni and NiTi. *Adv. Eng. Mater.* 2021; 23(11):2100159.
12. Pandey KK, Levitas VI, Park C. Effect of the initial microstructure on the pressure-induced phase transition in Zr and microstructure evolution. 2023. 25 p. Located at: <https://arxiv.org/abs/2301.10475>
13. Zepeda-Ruiz LA, Stukowski A, Ooppelstrup T, et al. Probing the limits of metal plasticity with molecular dynamics simulations. *Nature* 2017; 550(7677):492-495.
14. Lin F, Hilairet N, Raterron P, et al. Elasto-viscoplastic self consistent modeling of the ambient temperature plastic behavior of periclase deformed up to 5.4 GPa. *J. Appl. Phys.* 2017; 122(20):205902.
15. Meade C, Jeanloz R. The strength of mantle silicates at high pressures and room temperature: implications for the viscosity of the mantle. *Nature* 1990; 348:533-535.
16. Meade C, Jeanloz R. Effect of a coordination change on the strength of amorphous SiO<sub>2</sub>. *Science* 1988; 241(4869):1072-1074.
17. Levitas VI. Large Deformation of Materials with Complex Rheological Properties at Normal and High Pressure. New York (NY): Nova Science; 1996.
18. Pandey KK, Levitas VI. In situ quantitative study of plastic strain-induced phase transformations under high pressure: Example for ultra-pure Zr. *Acta Mater.* 2020;



196:338-346.

19. Levitas VI, Kamrani M, Feng B. Tensorial stress-strain fields and large elastoplasticity as well as friction in diamond anvil cell up to 400 GPa. *Npj Comput. Mater.* 2019; 5(1):94.
20. Hammersley AP. FIT2D: an introduction and overview. European synchrotron radiation facility internal report ESRF97HA02T 1997; 68:58.
21. Lutterotti L, Matthies S, Wenk HR, et al. Combined texture and structure analysis of deformed limestone from time-of-flight neutron diffraction spectra. *J. Appl. Phys.* 1997; 81(2):594-600.
22. Williamson GK, Smallman RE. III. Dislocation densities in some annealed and cold-worked metals from measurements on the X-ray debye-scherrer spectrum. *Philos. Mag.* 1956; 1(1):34-46.
23. Pérez-Prado MT, Zhilyaev AP. First experimental observation of shear induced hcp to bcc transformation in pure Zr. *Phys. Rev. Lett.* 2009; 102(17):175504.
24. Levitas VI, Zarechnyy OM. Modeling and simulation of strain-induced phase transformations under compression in a diamond anvil cell. *Phys. Rev. B* 2010; 82(17):174123.
25. Levitas VI, Dhar A, Pandey KK. Tensorial stress-plastic strain fields in  $\alpha$ - $\omega$  Zr mixture, transformation kinetics, and friction in diamond anvil cell. 2023. 32 p. Located at: <https://doi.org/10.48550/arXiv.2212.13000>
26. Kamrani M, Levitas VI, Feng B. FEM simulation of large deformation of copper in the quasi-constrain high-pressure-torsion setup. *Mat. Sci. Eng. A* 2017; 705:219-230.
27. Feng B, Levitas VI. Plastic flows and strain-induced alpha to omega phase transformation in zirconium during compression in a diamond anvil cell: finite element simulations. *Mater. Sci. Eng., A* 2017; 680:130-140.
28. Ji C, Levitas VI, Zhu H, et al. Shear-induced phase transition of nanocrystalline hexagonal boron nitride to wurtzitic structure at room temperature and lower pressure. *Proc. Natl. Acad. Sci. U. S. A.* 2012; 109(47):19108-19112
29. Gao Y, Ma Y, An Q, et al. Shear driven formation of nano-diamonds at sub-gigapascals and 300 K. *Carbon* 2019; 146:364-368.
30. Levitas VI. High-pressure phase transformations under severe plastic deformation by torsion in rotational anvils. *Mater. Trans.* 2019; 60(7):1294-1301.
31. Jenei Z, O'Bannon EF, Weir ST, et al. Single crystal toroidal diamond anvils for high pressure experiments beyond 5 megabar. *Nat. Commun.* 2018; 9(1):3563.

## Supplementary Material

### **In-situ study of rules of nanostructure evolution, severe plastic deformations, and friction under high pressure**

*Feng Lin\*, Valery I. Levitas\*, Krishan K. Pandey, Sorb Yesudhas, and Changyong Park*

#### **Contents:**

##### **Supplementary Methods**

1. Evaluation of yield strength under high pressure
2. Derivation of the advanced averaged equilibrium equation
3. Dislocation density estimation

##### **Supplementary Discussion**

##### **Supplementary Figures**

##### **References**

## Supplementary Methods

### 1. Evaluation of the yield strength under high pressure

Pressure dependence of the yield strength is of great interest to many disciplines for various reasons. It determines:

(a) strength of structural elements working under extreme loads, in particular, different high-pressure apparatuses, including DAC, rotational DAC, and apparatuses with metallic or ceramic dies for high-pressure torsion;

(b) the maximum pressure that can be achieved in materials compressed in DAC (see Equation (1));

(c) material flow in different technologies, like high-pressure material synthesis, extrusion, forging, cutting, polishing, and ball milling;

(d) maximum possible friction in heavily loaded contacts and related wear;

(e) the level of shear (deviatoric) stresses that can be applied to materials. The shear stresses drastically affect the phase transformations, chemical reactions, and other structural changes [1, 2, 18, 23, 28-30, 32, 33];

(f) plastic flow and geodynamic processes in Earth and other planets, including earthquakes.

There are two approaches to estimate yield strength under pressure in a DAC-like device, which exploit x-ray diffraction in either radial or axial diffraction geometry. With radial diffraction geometry, the yield strength in compression can be estimated from the lattice strains (distortion of crystal lattice planes) measured by synchrotron x-ray diffraction. Since the compression direction is perpendicular to the x-ray beam, lattice strains are detectable because axial compression symmetry and diffraction symmetry do not coincide. With this method, all the components of the elastic strain tensor in single crystals comprising polycrystalline samples can be determined. Combined with high-pressure single-crystal elastic constants, lattice strains can be used to estimate yield strength with proper mechanical assumptions [34]. Despite obtaining a large amount of experimental information and broad usage, this method suffers from several disadvantages:

(a) All measurements are averaged over the diameter of the sample, and the radial gradient of strain and stress fields is unavoidable due to contact friction. The macroscopic stress state also includes shear stresses, which are not included in the treatment. To reduce the

effect of friction, a relatively small ratio of the sample diameter to thickness  $d/h$  needs to be used, which also limits the axial displacement and applied plastic strain.

(b) When estimating yield strength from the lattice strains, different chosen mechanical assumptions to determine effective elastic properties of the polycrystalline aggregate (Reuss, Voigt, Hill, self-consistent, etc.) leads to different results.

(c) For multiphase materials, lattice strains give an estimation of stress in a single phase only. The mixture theory for the yield strength of multiphase material is not well developed, especially for the large difference in the yield strength of phases [35, 36].

(d) Yield strength depends on the pressure, plastic strain, and grain size that evolve during deformation. By presenting the yield strength versus pressure, all these effects are prescribed to the pressure only, which introduces large errors.

With axial diffraction geometry, yield strength is estimated using radial pressure gradient and sample thickness based on the simplified mechanical equilibrium equation in radial direction  $r$  [15-17], combined with the assumption that the friction stress reaches the yield strength in shear  $\tau_y$ :

$$\frac{d\bar{p}}{dr} = -\frac{2\tau_y(p)}{h}, \quad (\text{S1})$$

where  $\bar{p}$  is the pressure, averaged over the sample thickness. Previously, the pressure was measured at the surface using the ruby fluorescence method, and thickness was measured on recovered samples after unloading. Currently, pressure  $\bar{p}$  can be measured using x-ray diffraction and thickness using x-ray absorption. The advantage of Equation (S1) is that it does not include constitutive equations and assumptions, making it available for multiphase material. Disadvantages are:

(a) Due to the low friction coefficient of the diamond, the friction stress is much lower than the yield strength in shear  $\tau_y$ . This is the reason why this method significantly underestimates the yield strength.

(b) Stress  $\sigma$  and strain  $\epsilon_p$  tensor fields are strongly heterogeneous along the radius, and material undergoes very different plastic straining path  $\epsilon_p^{path}$  at different positions. Since the yield strength depends on pressure,  $\epsilon_p$ , and  $\epsilon_p^{path}$ , but is presented as a function of pressure only, this also introduces large errors.

(c) Equation (S1) neglects heterogeneity along the thickness and difference between pressure and normal stresses.

We eliminate all the above drawbacks and advance mechanical equilibrium Equation (S1) to the form of Equation (1) from the main text, which considers the heterogeneity of all stresses across the sample thickness, in the following part.

## 2. Derivation of the advanced averaged equilibrium equation

*Problem formulation.* For compression of a sample in the DAC,  $\sigma_{33}$ ,  $\sigma_{11}$ , and  $\sigma_{22}$  are the normal stress components along the load (vertical), radial, and azimuthal directions, respectively;  $\tau_{31}$  is the shear stress;  $\sigma_y$  and  $\tau_y$  are the yield strength in compression and shear respectively. Compressive stresses are negative. Pressure is defined as:

$$p = -(\sigma_{11} + \sigma_{22} + \sigma_{33})/3. \quad (\text{S2})$$

All stresses and pressure are functions of  $r$  and  $2z/h$  in a cylinder coordinate system with the origin at the center of the sample cylinder, where  $h$  is the sample thickness; in particular,  $p(0)$  corresponds to the symmetry plane  $z = 0$  and  $p(1)$  corresponds to the contact surface  $2z/h = 1$ . Pressure (or any stress), averaged over the sample thickness, is defined as:

$$\bar{p} = \frac{1}{h} \int_0^h p \, dz. \quad (\text{S3})$$

The contact friction stress  $\tau_f$  is defined by the simplified mechanical equilibrium equation.

$$\frac{d\bar{\sigma}_{11}}{dr} = -\frac{2\tau_f(p(1))}{h}. \quad (\text{S4})$$

The pressure-dependent yield strength in compression  $\sigma_y$  and shear  $\tau_y = \sigma_y/\sqrt{3}$  (based on the von Mises equivalent stress) are:

$$\sigma_y = \sigma_y^0 + bp; \quad \tau_y = \sigma_y/\sqrt{3} = (\sigma_y^0 + bp)/\sqrt{3}. \quad (\text{S5})$$

Note that  $\sigma_y$  depends on the local pressure  $p$ . At the contact surface, symmetry plane, and for averaged over the thickness, we have different pressures and yield strengths:

$$\begin{aligned} \sigma_y(1) &= \sigma_y^0 + bp(1); & \sigma_y(0) &= \sigma_y^0 + bp(0); & \bar{\sigma}_y &= \sigma_y^0 + b\bar{p}. \\ \tau_y(1) &= (\sigma_y^0 + bp(1))/\sqrt{3}; & \tau_y(0) &= (\sigma_y^0 + bp(0))/\sqrt{3}; & \bar{\tau}_y &= (\sigma_y^0 + b\bar{p})/\sqrt{3}. \end{aligned} \quad (\text{S6})$$

For maximum possible friction provided by the rough-DA, we have:

$$\tau_f(p(1)) = \tau_y(1) = \frac{1}{\sqrt{3}} \sigma_y(1) = \frac{1}{\sqrt{3}} (\sigma_y^0 + bp(1)). \quad (\text{S7})$$

With expression in Equation (S7), the equilibrium Equation (S4) specifies as:

$$\frac{d\bar{\sigma}_{11}}{dr} = -\frac{2}{\sqrt{3}} \frac{\sigma_y(1)}{h} = -\frac{2}{\sqrt{3}} \frac{\sigma_y^0 + bp(1)}{h}. \quad (\text{S8})$$

Since we assume that in XRD experiments, the distribution of pressure  $\bar{p}(r)$  averaged over the thickness is measured, we need to express  $\bar{\sigma}_{11}$  and  $p(1)$  in Equation (S11) in terms of  $\bar{p}(r)$ . Traditionally, this difference is neglected, i.e., it is assumed  $\bar{\sigma}_{11} = p(1) = \bar{p}(r)$ , which introduces errors.

*Analytical evaluation of the stress and pressure fields.* We assume that the material behaves as perfectly plastic and isotropic macroscopically, with the surface of perfect plasticity  $\varphi(\mathbf{s}) = \sigma_y(p)$  in the 5D deviatoric stress tensor  $s$  space. This surface is independent of the plastic strain tensor  $\boldsymbol{\varepsilon}_p$  and its path  $\boldsymbol{\varepsilon}_p^{path}$ . Such behavior can be achieved after large enough preliminary plastic deformation leading to saturation of hardness [17]. The pressure-dependent von Mises yield condition (i.e., Drucker-Prager yield condition) is assumed:

$$\varphi(\mathbf{s}) = \frac{1}{\sqrt{2}} \sqrt{(\sigma_{11} - \sigma_{22})^2 + (\sigma_{11} - \sigma_{33})^2 + (\sigma_{22} - \sigma_{33})^2 + 6\tau_{13}^2} = \sigma_y(p) = \sqrt{3}\tau_y(p). \quad (\text{S9})$$

Equilibrium equations are:

$$\frac{\partial \sigma_{11}}{\partial r} + \frac{\partial \tau_{13}}{\partial z} + \frac{\sigma_{11} - \sigma_{22}}{r} = 0; \quad (\text{S10})$$

$$\frac{\partial \sigma_{33}}{\partial z} + \frac{\partial \tau_{13}}{\partial r} + \frac{\tau_{13}}{r} = 0. \quad (\text{S11})$$

The following assumptions are made:

(a) It approximately follows from the finite element method simulations and DAC experiments:  $\sigma_{11} = \sigma_{22}$ . Then plasticity condition Equation (S9) simplifies to:

$$(\sigma_{11} - \sigma_{33})^2 + 3\tau_{31}^2 = \sigma_y^2(p) = 3\tau_y^2(p). \quad (\text{S12})$$

(b) Stress  $\sigma_{33}$  is independent of  $z$ . However, it does not mean that:

$$\frac{\partial \tau_{13}}{\partial r} + \frac{\tau_{13}}{r} = 0 \quad \rightarrow \quad \tau_{13} = \tau_0(z) \frac{r_0}{r}. \quad (\text{S13})$$

because at the contact surface,  $\tau_0(z)$  may equal constant  $\sigma_y$  for all  $r$  for material with pressure-independent yield strength.  $\sigma_{33}$  that is independent of  $z$  means two other terms in Equation (S11) make small contributions to  $\sigma_{33}$ .

For plane strain, when the term  $\frac{\tau_{13}}{r}$  in Equation (S11) is absent, a slightly modified Prandtl's solution for the maximum possible contact friction [37] for stresses that satisfy equilibrium equations and plasticity conditions are:

$$\frac{\sigma_{33}(r)}{\tau_y} = \frac{\sigma_{33}(0)}{\tau_y} + \frac{2r}{h}; \quad (\text{S14})$$

$$\frac{\tau_{13}}{\tau_y} = \frac{2z}{h}, \quad (\text{S15})$$

$$\frac{\sigma_{11}}{\tau_y} = \frac{\sigma_{33}(0)}{\tau_y} + \frac{2r}{h} + \sqrt{3} \sqrt{1 - \left(\frac{2z}{h}\right)^2} = \frac{\sigma_{33}(r)}{\tau_y} + \sqrt{3} \sqrt{1 - \left(\frac{2z}{h}\right)^2}; \quad (\text{S16})$$

$$\frac{p}{\tau_y} = -\frac{2\sigma_{11} + \sigma_{33}}{3\tau_y} = -\frac{\sigma_{33}(r)}{\tau_y} - \frac{2}{3} \sqrt{3} \sqrt{1 - \left(\frac{2z}{h}\right)^2}. \quad (\text{S17})$$

The difference with Prandtl's solution is in multiplier  $\sqrt{3}$  instead of 2 in Equation (6) for  $\sigma_{11}$ . The reason is that we use the von Mises condition and  $\sigma_{11} = \sigma_{22}$ , which results in Equation (S12), while in Prandtl's solution, the Tresca condition along with plane strain assumption leads to the yield condition  $(\sigma_{11} - \sigma_{33})^2 + 4\tau_{31}^2 = \sigma_y^2 = 4\tau_y^2$ .

Equation (S16) and Equation (S17) lead to the relationship:

$$\frac{\sigma_{11}}{\tau_y} = -\frac{p}{\tau_y} + \frac{\sqrt{3}}{3} \sqrt{1 - \left(\frac{2z}{h}\right)^2}. \quad (\text{S18})$$

Stress  $\bar{\sigma}_{11}$  and pressure  $\bar{p}$ , averaged over the sample thickness are

$$\frac{\bar{\sigma}_{11}}{\tau_y(\bar{p})} = \frac{1}{h} \int_0^h \frac{\sigma_{11}}{\tau_y} dz = \frac{\sigma_{33}(0)}{\tau_y(\bar{p})} + \frac{2r}{h} + \frac{\sqrt{3}\pi}{4} = \frac{\sigma_{33}}{\tau_y(\bar{p})} + \frac{\sqrt{3}\pi}{4}; \quad (\text{S19})$$

$$\frac{\bar{p}}{\tau_y(\bar{p})} = -\frac{\sigma_{33}}{\tau_y(\bar{p})} - \frac{\sqrt{3}\pi}{6}. \quad (\text{S20})$$

We assumed that  $\tau_y$  is constant during averaging and then substituted in the result  $\tau_y(\bar{p})$ . It is possible to avoid this assumption, but the final equations are getting too bulky and unusable analytically for our purposes. Note that the averaged value of  $\bar{\sigma}_{11}$  is much closer to the value of  $\sigma_{11}(2z/h)$  at the symmetry plane  $\sigma_{11}(0)$  than at the contact surface  $\sigma_{11}(1)$ . For example,  $(\sigma_{11}(0) - \sigma_{33})/(\sqrt{3}\tau_y) = 1$ ,  $\sigma_{11}(1) - \sigma_{33} = 0$ , and  $(\bar{\sigma}_{11} - \sigma_{33})/(\sqrt{3}\tau_y) = 0.79$ . Similar,  $(p(0) + \sigma_{33})/(2\tau_y/\sqrt{3}) = -1$ ,  $p(1) - \sigma_{33} = 0$ , and  $(\bar{\sigma}_{11} - \sigma_{33})/(2\tau_y/\sqrt{3}) = -0.79$ .

Equation (S19) and Equation (S20) lead to the relationship:

$$\frac{\bar{\sigma}_{11}}{\tau_y(\bar{p})} = -\frac{\bar{p}}{\tau_y(\bar{p})} + \frac{\sqrt{3}\pi}{12}. \quad (\text{S21})$$

We aim to find the relationship between  $\bar{\sigma}_{11}$ ,  $\sigma_{11}(0)$ , and  $\sigma_{11}(1)$ . We will use the following identity:

$$\bar{\sigma}_{11} = \sigma_{11}(1)w + \sigma_{11}(0)(1 - w); \quad w := \frac{\bar{\sigma}_{11} - \sigma_{11}(0)}{\sigma_{11}(1) - \sigma_{11}(0)}. \quad (\text{S22})$$

Where  $w$  is treated as the weight factor. Utilizing Equation (S16) and Equation (S19), we obtain:

$$w = 1 - \frac{\pi}{4} \frac{\sigma_y(\bar{p})}{\sigma_y(p(0))} = 1 - \frac{\pi}{4} \frac{\sigma_y^0 + b\bar{p}}{\sigma_y^0 + bp(0)}. \quad (\text{S23})$$

Similar,

$$\bar{p} = p(1)w + p(0)(1 - w); \quad w = \frac{\bar{p} - p(0)}{p(1) - p(0)}. \quad (\text{S24})$$

Here we used the same symbol  $w$  because, from Equation (S17) and Equation (S20), it has the same expression (Equation (S23)) as for  $\sigma_{11}$ . Also, we obtain from Equation (S16) and Equation (S18):

$$\sigma_{11}(1) = -p(1) = \sigma_{33}; \quad \sigma_{11}(0) = -p(0) + \frac{\sqrt{3}}{3} \tau_y(p(0)) = -p(0) + \frac{1}{3} \sigma_y(p(0)); \quad (\text{S25})$$

from Equation (S17):

$$p(0) = -\sigma_{33} - 1.155 \tau_y(p(0)) = -\sigma_{33} - 0.667 \sigma_y(p(0)) = p(1) - 0.667 \sigma_y(p(0)); \quad (\text{S26})$$

from Equation (S21):

$$\bar{\sigma}_{11} = -\bar{p} + 0.453 \tau_y(\bar{p}) = -\bar{p} + 0.262 \sigma_y(\bar{p}) = 0.262 \sigma_y^0 + \bar{p}(0.262b - 1). \quad (\text{S27})$$

Elaborating Equation (S26) with allowing for Equation (S6):

$$p(0) = p(1) - 0.667 \sigma_y(p(0)) = p(1) - 0.667 [\sigma_y^0 + bp(0)] \rightarrow p(0) = \frac{p(1) - 0.667 \sigma_y^0}{1 + 0.667b}. \quad (\text{S28})$$

Substitution of Equation (S28) in Equation (S23) and Equation (S24) results in:

$$\bar{p} = p(1)w + \frac{p(1) - 0.667 \sigma_y^0}{1 + 0.667b} (1 - w); \quad w = 1 - (0.785 + 0.524b) \frac{\sigma_y^0 + b\bar{p}}{\sigma_y^0 + bp(1)}. \quad (\text{S29})$$

Resolving linear equations Equation (S29) for  $w$  and  $p(1)$ , we obtain:

$$w = \frac{0.411}{1.910 + b}; \quad (\text{S30})$$

$$p(1) = 0.524 \sigma_y^0 + (1 + 0.524b) \bar{p}. \quad (\text{S31})$$

Substituting in Equation (S6) for  $\sigma_y(1)$  in Equation (S31), we obtain:

$$\sigma_y(1) = \sigma_y^0 + bp(1) = (\sigma_y^0 + b\bar{p})(1 + 0.524b) \quad (\text{S32})$$

Substituting Equation (S27) and Equation (S32) in Equation (S8) results in the final equilibrium equation for parameters  $\sigma_y^0$  and  $b$  from the best fit to experiments:

$$\frac{d\bar{p}}{dr} = -\frac{2}{\sqrt{3}} \frac{1 + 0.524b}{1 - 0.262b} \frac{\sigma_y^0 + b\bar{p}}{h}. \quad (\text{S33})$$

Equation (S33) is the final mechanical equilibrium equation expressed in terms of measured pressure  $\bar{p}$  averaged of the sample thickness, which is used as Equation (1) in the main text to determine the pressure dependence of the yield strength. It transforms to the known Equation [15-17] for  $b = 0$  only. We want to use data from all four compression stages as a single data set. To do this, we must justify a way to combine all data in a single plot. Equation (S33) and its solution in Equation (1) in the main text have the following properties:

(a) Pressure distribution depends on the dimensionless geometric parameter  $r/h$  rather than on  $r$  and  $h$  separately.



(b) Pressure distribution curves for different applied forces and compression can be overlapped by shifting curves along the  $r$ -axis without changing  $\sigma_y(p)$ , since change  $r \rightarrow r + C$  does not violate Equation (S33). Indeed, one can choose the same  $p_0$  for all curves and choose constant  $C$  for each curve such that  $\frac{r+C}{h} = \text{const}$  is the same for all curves.

These properties are used in Figure 3 in the main text. Practically, one can choose a fixed  $(p_f, r_f)$  point in the  $p - r/h$  plane for all curves to pass through. Then the curve that originally passes through the point  $(p_f, r_i)$ , should be shifted in the positive direction by the distance  $(r_f - r_i)/h$ , so that the new curve passes through  $(p_f, r_f)$ . Then we used all the points in the shifted curve in Figure 3 to find the best fit for Equation (S33) (or Equation (1) in the main text).

### 3. Dislocation density estimation

The crystallite sizes and microstrains extracted from the refinement using MAUD were used to estimate the dislocation density. Dislocation density can be expressed as [22]:

$$\rho = \sqrt{\rho_c \rho_{ms}}. \quad (\text{S34})$$

where  $\rho_c$  and  $\rho_{ms}$  are the contribution to overall dislocation density from crystallite size and microstrain, respectively. Contribution from crystallite size is:

$$\rho_c = \frac{3}{d^2}. \quad (\text{S35})$$

Where  $d$  is crystallite size. Contribution from the microstrain is determined by the Equation:

$$\rho_{ms} = k\varepsilon^2/b^2. \quad (\text{S36})$$

Where  $\varepsilon$  is the microstrain;  $b$  is the magnitude of the Burgers vector;  $k = 6\pi A \left( \frac{E}{G \ln(r/r_0)} \right)$  is a material constant;  $E$  and  $G$  are Young's modulus and shear modulus, respectively;  $A$  is a constant that lies between 2 and  $\pi/2$  based on the distribution of strain;  $r$  is the radius of crystallite with dislocation;  $r_0$  is a chosen integration limit for dislocation core. In this study,  $A = \pi/2$  is the gaussian distribution of strain. Moduli  $E$ ,  $G$  and their pressure dependence for  $\omega$ -Zr are taken from [38], respectively. A reasonable value of  $\ln(r/r_0)$  being 4 is used [22].  $\alpha$ -Zr has a dominant prismatic slip system of  $\{1\bar{1}00\}\{11\bar{2}0\}$  [39-42]. For  $\omega$ -Zr, a prismatic  $\{11\bar{2}0\}\{1\bar{1}00\}$  and basal  $\{0001\}\{1\bar{1}00\}$  dominant slip system is suggested based on plasticity modeling [43]. Since the crystal lattice gets compressed under pressure, the length of the Burger vector is calculated using pressure-dependent lattice constants. It is worth to note that when estimating dislocation density using the Williamson-Smallman method, we only consider one dominant dislocation slip system. However, to accommodate arbitrarily

imposing plastic strain on polycrystals, auxiliary slip systems are usually needed. With changing orientation of grains during deformation, the Schmid factor of slip systems changes, and thus slip system activities, which is the percentage of plastic strain accommodated by certain slip systems, will be different. This may induce uncertainty in dislocation density estimation.

## **Supplementary Discussion**

### **1. Scatter in crystallite size and dislocation density in $\omega$ -Zr after completing phase transformation**

While the crystallite size and the dislocation density in  $\omega$ -Zr after completing the phase transformation are independent of the radius (Figure 4), there are some scatters around the average along the radius. Also, the dislocation densities vary slightly between 6, 10, and 14 GPa steps. These scatters cannot be attributed to the dependence of the crystallite size and dislocation density on pressure, plastic strain, and strain path. Indeed, pressure strongly and monotonously reduces, plastic strain strongly and monotonously increases along the radius, and the plastic strain path also changes monotonically. However, there is no clear radial dependence of the crystallite size and the dislocation density. Because of the large fluctuation, the slight difference in the average dislocation density between 6, 10, and 14 GPa steps also cannot be solely attributed to the growing pressure and plastic strain. A possibility is that the observed fluctuations in the crystallite size and the dislocation density after PT completed are due to evolving texture (i.e., dynamically changing distribution of crystallographic orientations and uncharacterized preferred orientations) during the plastic deformation with increasing pressure and errors in post-processing of XRD patterns as described in dislocation density estimation section.

### **2. Relationship between the yield surface and surface of perfect plasticity**

Our results provide the first quantitative proof of the fixed isotropic pressure-dependent surface of perfect plasticity independent of  $\epsilon_p$  and  $\epsilon_p^{path}$ , which is far beyond the observation and description in terms of the 'steady hardness'. However, it is well-known that severely deformed materials exhibit plastic strain-induced texture and anisotropy, including the

Bauschinger effect described by back stresses. Thus, the traditional yield surface is evolving, anisotropic, and depends on  $\boldsymbol{\varepsilon}_p$  and  $\boldsymbol{\varepsilon}_p^{path}$  (Figure 2). To resolve this seeming contradiction, we use two different surfaces in “5D” space of deviatoric stresses  $\boldsymbol{s}$  at fixed  $p$ : traditional evolving anisotropic yield surface  $f(\boldsymbol{s}, \boldsymbol{\varepsilon}_p, \boldsymbol{\varepsilon}_p^{path}) = \sigma_y(p)$  and fixed isotropic surface of perfect plasticity  $\varphi(\boldsymbol{s}) = \sigma_y(p)$ . After some critical plastic strain, the yield surface reaches  $\varphi(\boldsymbol{s}) = \sigma_y(p)$ , and at further monotonous loading, it moves with the deviatoric stress vector  $\boldsymbol{s}$  along the fixed isotropic surface  $\varphi(\boldsymbol{s}) = \sigma_y(p)$ . Thus, the material deforms like perfectly plastic, isotropic with the fixed surface of perfect plasticity. However, during sharp change in loading direction or unloading and reloading in a different direction in the stress space, flow occurs in accordance with actual evolving anisotropic yield surface  $f(\boldsymbol{s}, \boldsymbol{\varepsilon}_p, \boldsymbol{\varepsilon}_p^{path}) = \sigma_y(p)$ . Due to limited measurement capabilities and strongly heterogeneous fields, and the complexity of equation  $f(\boldsymbol{s}, \boldsymbol{\varepsilon}_p, \boldsymbol{\varepsilon}_p^{path}) = \sigma_y(p)$ , it is impossible to determine it experimentally. However, finding the surface of perfect plasticity  $\varphi(\boldsymbol{s}) = \sigma_y(p)$  is very important because it fully characterizes material's behavior after some critical level of severe plastic deformation and for monotonous loading. Note that the isotropy of the surface of perfect plasticity  $\varphi(\boldsymbol{s}) = \sigma_y(p)$  follows not only from experiments but from the theory. Indeed, since initially polycrystalline material with stochastic grain orientation without texture is isotropic, its anisotropy during deformation can come from  $\boldsymbol{\varepsilon}_p$  and  $\boldsymbol{\varepsilon}_p^{path}$  only, i.e., it is strain-induced. Since  $\varphi(\boldsymbol{s}) = \sigma_y(p)$  is independent of  $\boldsymbol{\varepsilon}_p$  and  $\boldsymbol{\varepsilon}_p^{path}$ , the only source for anisotropy disappears.

## Supplementary Figures

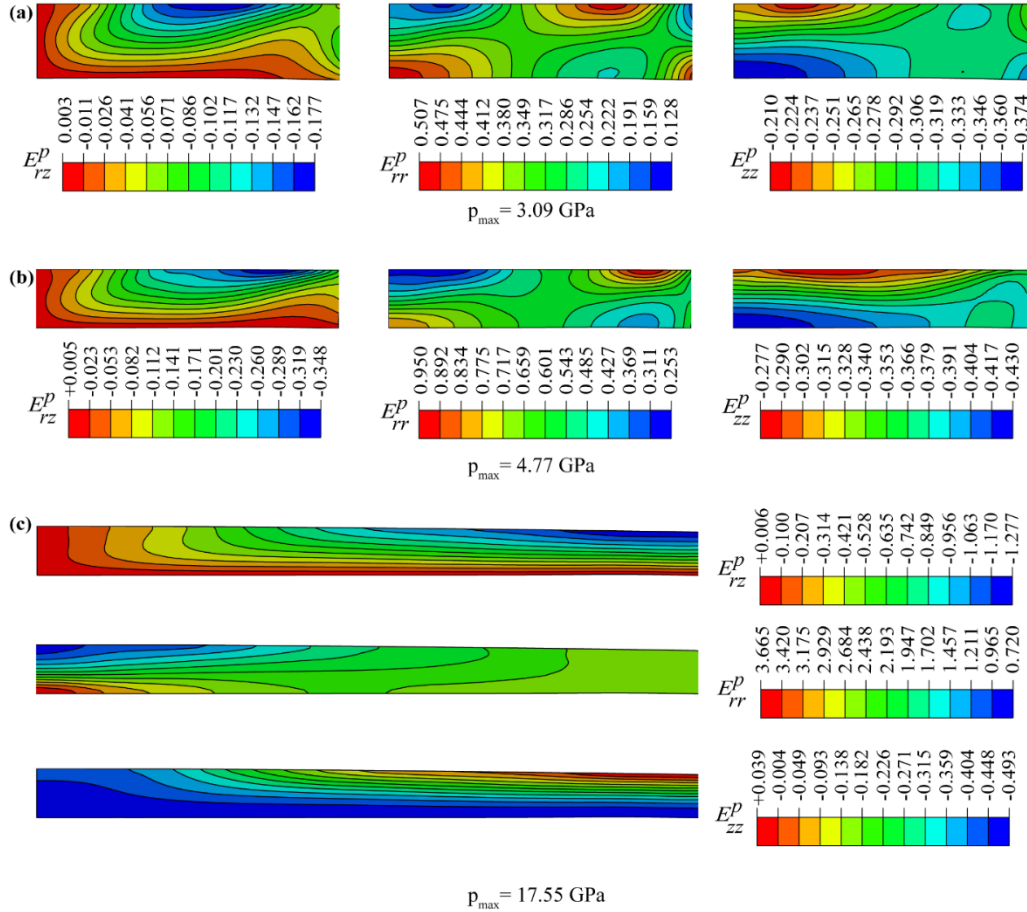


**Figure S1. Distributions of components of Lagrangian plastic strains in a quarter of a sample for three loadings characterized by the maximum pressure in a sample.** Very heterogeneous and nontrivial distributions are observed, caused by heterogeneous contact friction. At the symmetry axis (left side of a sample) and symmetry plane (bottom of a sample) shear strains  $E_{rz}^p$  are zero. At the contact surface with a diamond (top of a sample), shear strains and particle rotations reach their maximum due to large contact friction. During compression, each material particle flows radially in the region with larger shear and different proportions of the normal strain, i.e., is subjected to complex nonproportional straining, very different from other particles. Thus, numerous plastic strain tensors and straining paths are realized. Adopted with changes from [25] with permissions.

## Reference

1. Edalati K, Bachmaier A, Beloshenko VA, et al. Nanomaterials by severe plastic deformation: review of historical developments and recent advances. *Mater. Res. Lett.* 2022; 10(4):163-256.
2. Edalati K, Horita K. A review on high-pressure torsion (HPT) from 1935 to 1988. *Mater. Sci. Eng., A.* 2016; 652:325-352.
3. Razumov, IK, Yermakov AY, Gornostyrev YN, et al. Nonequilibrium phase transformations in alloys under severe plastic deformation. *Phys.-Usp.* 2020; 63(8):733.
4. Cao Y, Ni S, Liao X, et al. Structural evolutions of metallic materials processed by severe plastic deformation. *Mater. Sci. Eng. R Rep.* 2018; 133:1-59.
5. Valiev RZ, Estrin Y, Horita Z, et al. Producing bulk ultrafine-grained materials by severe plastic deformation. *JOM* 2006; 58:33-39.
6. Ovid'Ko IA, Valiev RZ, Zhu YT. Review on superior strength and enhanced ductility of metallic nanomaterials. *Prog. Mater. Sci.* 2018; 94:462-540.
7. Valiev RZ, Estrin Y, Horita Z, et al. Producing bulk ultrafine-grained materials by severe plastic deformation: ten years later. *JOM* 2016; 68:1216-1226.
8. Zhu YT, Langdon TG. The fundamentals of nanostructured materials processed by severe plastic deformation. *JOM* 2004; 56(10):58-63.
9. Girard J, Amulele G, Farla R, et al. Shear deformation of bridgmanite and magnesiowüstite aggregates at lower mantle conditions. *Science* 2016; 351(6269):144-147.
10. Levitas VI. Resolving puzzles of the phase-transformation-based mechanism of the strong deep-focus earthquake. *Nat. Commun.* 2022; 13(1):6291.
11. Kerber MB, Spieckermann F, Schuster R, et al. In Situ Synchrotron X-Ray Diffraction during High-Pressure Torsion Deformation of Ni and NiTi. *Adv. Eng. Mater.* 2021; 23(11):2100159.
12. Pandey KK, Levitas VI, Park C. Effect of the initial microstructure on the pressure-induced phase transition in Zr and microstructure evolution. 2023. 25 p. Located at: <https://arxiv.org/abs/2301.10475>
13. Zepeda-Ruiz LA, Stukowski A, Ooppelstrup T, et al. Probing the limits of metal plasticity with molecular dynamics simulations. *Nature* 2017; 550(7677):492-495.
14. Lin F, Hilairet N, Raterron P, et al. Elasto-viscoplastic self consistent modeling of the

ambient temperature plastic behavior of periclase deformed up to 5.4 GPa. *J. Appl. Phys.* 2017; 122(20):205902.

15. Meade C, Jeanloz R. The strength of mantle silicates at high pressures and room temperature: implications for the viscosity of the mantle. *Nature* 1990; 348:533-535.

16. Meade C, Jeanloz R. Effect of a coordination change on the strength of amorphous SiO<sub>2</sub>. *Science* 1988; 241(4869):1072-1074.

17. Levitas VI. *Large Deformation of Materials with Complex Rheological Properties at Normal and High Pressure*. New York (NY): Nova Science; 1996.

18. Pandey KK, Levitas VI. In situ quantitative study of plastic strain-induced phase transformations under high pressure: Example for ultra-pure Zr. *Acta Mater.* 2020; 196:338-346.

19. Levitas VI, Kamrani M, Feng B, et al. Tensorial stress-strain fields and large elastoplasticity as well as friction in diamond anvil cell up to 400 GPa. *Npj Comput. Mater.* 2019; 5(1):94.

20. Hammersley AP. FIT2D: an introduction and overview. European synchrotron radiation facility internal report ESRF97HA02T 1997; 68:58.

21. Lutterotti L, Matthies S, Wenk HR, et al. Combined texture and structure analysis of deformed limestone from time-of-flight neutron diffraction spectra. *J. Appl. Phys.* 1997; 81(2):594-600.

22. Williamson GK, Smallman RE. III. Dislocation densities in some annealed and cold-worked metals from measurements on the X-ray debye-scherrer spectrum. *Philos. Mag.* 1956; 1(1):34-46.

23. Pérez-Prado MT, Zhilyaev AP. First experimental observation of shear induced hcp to bcc transformation in pure Zr. *Phys. Rev. Lett.* 2009; 102(17):175504.

24. Levitas VI, Zarechnyy OM. Modeling and simulation of strain-induced phase transformations under compression in a diamond anvil cell. *Phys. Rev. B* 2010; 82(17):174123.

25. Levitas VI, Dhar A, Pandey KK. Tensorial stress-plastic strain fields in  $\alpha$ - $\omega$  Zr mixture, transformation kinetics, and friction in diamond anvil cell. 2023. 32 p. Located at: <https://doi.org/10.48550/arXiv.2212.13000>

26. Kamrani M, Levitas VI, Feng B. FEM simulation of large deformation of copper in the quasi-constrain high-pressure-torsion setup. *Mat. Sci. Eng. A* 2017; 705:219-230.

27. Feng B, Levitas VI. Plastic flows and strain-induced alpha to omega phase transformation in zirconium during compression in a diamond anvil cell: finite element simulations. *Mater. Sci. Eng., A* 2017; 680:130-140.
28. Ji C, Levitas VI, Zhu H, et al. Shear-induced phase transition of nanocrystalline hexagonal boron nitride to wurtzitic structure at room temperature and lower pressure. *Proc. Natl. Acad. Sci. U. S. A.* 2012; 109(47):19108-19112
29. Gao Y, Ma Y, An Q, et al. Shear driven formation of nano-diamonds at sub-gigapascals and 300 K. *Carbon* 2019; 146:364-368.
30. Levitas VI. High-pressure phase transformations under severe plastic deformation by torsion in rotational anvils. *Mater. Trans.* 2019; 60(7):1294-1301.
31. Jenei Z, O'Bannon EF, Weir ST, et al. Single crystal toroidal diamond anvils for high pressure experiments beyond 5 megabar. *Nat. Commun.* 2018; 9(1):3563.
32. Levitas VI, Shvedov LK. Low-pressure phase transformation from rhombohedral to cubic BN: experiment and theory. *Phys. Rev. B* 2002; 65(10):104109.
33. Levitas VI. High-pressure mechanochemistry: conceptual multiscale theory and interpretation of experiments. *Phys. Rev. B* 2004; 70(18), 184118.
34. Singh AK, Balasingh C, Mao HK, et al. Analysis of lattice strains measured under nonhydrostatic pressure. *J. Appl. Phys.* 1998; 83(12):7567-7575.
35. Handy MR. Flow laws for rocks containing two non-linear viscous phases: a phenomenological approach. *J. Struct. Geol.* 1994; 16(3):287-301.
36. Lin F, Giannetta M, Jugle M, et al. Texture development and stress-strain partitioning in periclase+ halite aggregates. *Minerals* 2019; 9(11):679.
37. Hill R. *The Mathematical Theory of Plasticity*. Oxford: Clarendon Press; 1998.
38. Liu W, Li B, Wang L, et al. Elasticity of  $\omega$ -phase zirconium. *Phys. Rev. B* 2007; 76(14):144107.
39. Capolungo L, Beyerlein IJ, Kaschner GC, et al. On the interaction between slip dislocations and twins in HCP Zr. *Mater. Sci. Eng., A* 2009; 513:42-51.
40. Kaschner GC, Tomé CN, Beyerlein IJ, et al. Role of twinning in the hardening response of zirconium during temperature reloads. *Acta Mater.* 2006; 54(11):2887-2896.
41. Tomé CN, Maudlin PJ, Lebensohn RA, et al. Mechanical response of zirconium—I.

Derivation of a polycrystal constitutive law and finite element analysis. *Acta Mater.* 2001; 49(15):3085-3096.

42. Knezevic M, Beyerlein IJ, Nizolek T, et al. Anomalous basal slip activity in zirconium under high-strain deformation. *Mater. Res. Lett.* 2013; 1(3):133-140.

43. Wenk HR, Kaercher P, Kanitpanyacharoen W, et al. Orientation relations during the  $\alpha$ - $\omega$  phase transition of zirconium: In situ texture observations at high pressure and temperature. *Phys. Rev. Lett.* 2013; 111(19):195701.